Anisotropic scattering rates in strain-tuned Sr_2RuO_4

Ben Currie,[1] David T. S. Perkins,[2] Evgeny Kozik,[1] Joseph J. Betouras,[2] and Jörg Schmalian[3,4]
[1]*Department of Physics, King's College London, Strand, London WC2R 2LS, United Kingdom*
[2]*Department of Physics, Loughborough University, Loughborough LE11 3TU, United Kingdom*
[3]*Institut für Theorie der Kondensierten Materie, Karlsruher Institut für Technologie, 76131 Karlsruhe, Germany*
[4]*Institut für Quantenmaterialien und Technologien, Karlsruher Institut für Technologie, 76131 Karlsruhe, Germany*

(Received 9 December 2025; revised 7 February 2026; accepted 12 February 2026; published 16 March 2026)

Motivated by recent angle-resolved photoemission spectroscopy (ARPES) experiments, we analyze the temperature, frequency, and momentum dependence of the single-particle scattering rate in a model of the γ-band of Sr_2RuO_4 under strain, with particular emphasis on the behavior near the Lifshitz transition where the Fermi energy crosses a single Van Hove point. While the scattering rate is only moderately anisotropic at zero strain, we find that it becomes strongly anisotropic at the Lifshitz point. At the lowest energies, we recover the expected universal behavior: the scattering rate varies (ignoring logarithmic corrections) as $\tau^{-1} \sim \omega$ at the Van Hove point and as $\tau^{-1} \sim \omega^{3/2}$ away from it. At higher energies, however, corrections of order ω^2 become important in both regimes. We show that the experimentally observed behavior $\tau^{-1} \sim \omega^{\alpha}$ with $\alpha \approx 1.4(2)$ at the Van Hove point can be quantitatively explained by a superposition of linear and quadratic contributions to the scattering rate, which are comparable in magnitude at the intermediate energies probed by experiment, rather than in terms of a new universal power law. We further predict a distinctive anisotropy, strain dependence, and a nonmonotonic frequency dependence of the scattering rate at a Lifshitz transition, all of which may be directly tested in experiments.

DOI: 10.1103/zjhr-xw73

I. INTRODUCTION

The role of electron-electron interactions in two-dimensional systems with a Van Hove singularity [1] (VHS) in the vicinity of the Fermi energy has received significant recent interest [2]. Materials in which the proximity to a Van Hove point is relevant include doped graphene [3–7], moiré materials [8–13], metallic kagome superconductors [14–17], $Sr_3Ru_2O_7$ in an external magnetic field [18], the bulk of Sr_2RuO_4 [19–22] under uniaxial compressive strain, and the surface of Sr_2RuO_4 [23,24]. In particular, the strain-tuned Lifshitz transition of Sr_2RuO_4 [25]—where the Fermi energy crosses a single, quasi-two-dimensional VHS—gives rise to a number of anomalies: At the transition, one finds a pronounced maximum of the superconducting transition temperature [19,26]; a giant lattice softening, as observed in a dramatic reduction of Young's modulus [27]; a well-established maximum in the electronic entropy, as revealed in measurements of the elastocaloric effect [21]; and deviations from the Fermi-liquid T^2-variation of the resistivity $\rho(T)$ [20,28]. For the lattermost example, transport experiments find an anomalous $T^2 \log T$ scaling of $\rho(T)$ at the Lifshitz transition [20,28], a behavior expected for a Fermi liquid tuned to a Van Hove point [22,29,30]. The Fermi surfaces of Sr_2RuO_4 at zero strain and at the strain-tuned Lifshitz point are shown in the left and right panels of Fig. 1, respectively, with each consisting of three sheets. Here we focus on the so-called γ-sheet, where the Fermi surface meets the Van Hove point at $\boldsymbol{k} = (0, \pm\pi)$ (indicated in color in Fig. 1).

The enhanced entropy and compressibility near the Lifshitz transition, as well as the pronounced lattice softening, are directly linked to a broad spectrum of particle-hole, *compressive* excitations at small momentum and characterized by the density response:

$$\mathrm{Im}\Pi(\boldsymbol{q},\omega) = -\frac{m}{2\pi}\begin{cases} \frac{\omega}{|\varepsilon_{\mathrm{VH}}(\boldsymbol{q})|} & \text{if} \quad |\omega| < |\varepsilon_{\mathrm{VH}}(\boldsymbol{q})|, \\ \mathrm{sgn}(\omega) & \text{if} \quad |\omega| > |\varepsilon_{\mathrm{VH}}(\boldsymbol{q})|, \end{cases} \tag{1}$$

where $\varepsilon_{\mathrm{VH}}(\boldsymbol{q}) = \frac{1}{2m}(q_x^2 - q_y^2)$ describes the dispersion near the Van Hove point. Notice, this is distinct from the behavior in systems with a spherical Fermi surface, where $\mathrm{Im}\Pi(\boldsymbol{q},\omega)$ is nonzero only for $|\omega| < v_F|\boldsymbol{q}|$, with v_F the Fermi velocity. The temperature and frequency dependence of the single-particle scattering rate $\tau_{\boldsymbol{k}}^{-1}(\omega, T)$ due to scattering off these soft fermionic compressive excitations is highly anisotropic along the Fermi surface. [For a definition of τ^{-1}, see Eq. (6).] For generic momenta away from the Van Hove point—called *cold* states and marked in blue in Fig. 1—$\tau^{-1} \propto \omega^{3/2}$ or $\propto T^{3/2}$ holds, whichever dominates [22,31]. On the other hand, in the immediate vicinity of the Van Hove point—called *hot* states and marked in red in Fig. 1—$\tau^{-1} \propto \omega/\log(D/\omega)$ or $\propto T/\log(D/T)$ holds, with bandwidth D [32–35]. These scattering events provide the dominant contribution to the

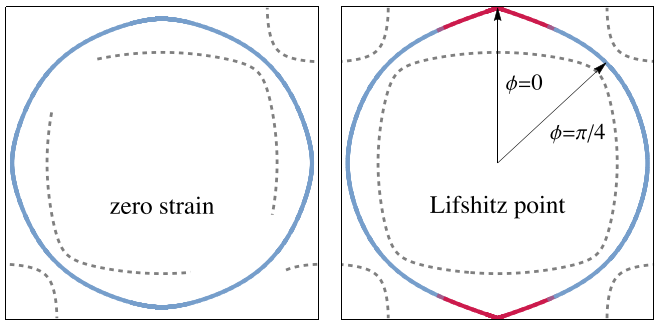

FIG. 1. Fermi surfaces in the first Brillouin zone of Sr_2RuO_4 at $k_z = 0$ for zero strain (left panel) and at the critical strain of the Lifshitz point (right panel). At the Lifshitz point, the γ-sheet of the Fermi surface (shown in color) touches the Van Hove point at in-plane momentum $\boldsymbol{k} = (0, \pm\pi)$. The part of the Fermi surface near the Van Hove point marked in red refers to the *hot* regions, while *cold* parts of the Fermi surface, away from the Van Hove point, are shown in blue. The angle ϕ marks the azimuthal angle relative to $(0, \pi)$. Dashed lines indicate the α- and β-sheets of the Fermi surface that are not analyzed in this paper.

single-particle self-energy, yet they are not relevant for the electrical resistivity in sufficiently clean systems, since scattering processes in a system with a single VHS at the Fermi energy have a small momentum transfer. In the absence of impurities, momentum is relaxed only by umklapp processes, which generally involve large transferred momenta. Hence, only mild deviations from the conventional Fermi liquid behavior occur in $\rho(T)$. These umklapp processes lead to the above-mentioned $T^2 \log T$ scaling of the resistivity [22,29,30]. In contrast, the thermal resistivity is sensitive to small-momentum scattering, and is predicted to obey a $T^{3/2}$ scaling [22]. The $\propto T/\log T$, non-Fermi-liquid-like behavior of hot carriers has been evasive and is generically hard to determine.

Recent angular-resolved photoemission spectroscopy (ARPES) measurements [36] found evidence that the quasiparticle spectral properties, specifically the single-particle scattering rate τ^{-1}, are strongly strain-dependent. At generic values of strain, the frequency dependence of τ^{-1} was found to obey the canonical Fermi liquid scaling $\tau^{-1}(\omega) \sim \omega^{\alpha}$ with $\alpha \approx 2$, similar to well-established quasiparticles seen at zero strain [23,37–40]. On the other hand, close to the critical strain of the Lifshitz transition, an anomalous scaling $\alpha = 1.4(2)$ was deduced right at the Van Hove point in the Brillouin zone. The ARPES experiments were conducted at a temperature $T = 11$ K, a regime below the coherence temperature $T_{\mathrm{FL}} \sim 25 - 40$ K of the unstrained samples [41–43].

While theory predicts a singular scattering, the exponent $\alpha = 1.4(2)$ obtained in Ref. [36] is distinct from the expected value of $\alpha = 1$. It raises the question of whether the scattering is indeed due to the broad continuum of compressive modes of Eq. (1), or whether one has to invoke additional interactions to explain this behavior, such as collective spin fluctuations, observed in inelastic neutron scattering experiments [44–49]. In this context, it is important to clarify whether the temperature and energy regimes probed in the ARPES measurements of Ref. [36] can indeed be considered as being in the ultimate low-T regime. This requires a quantitative analysis of the single-particle scattering processes that is based on a realistic modeling of the electronic structure. Clarifying which scattering processes dominate on the Fermi surface is also a key step toward identifying the mechanism responsible for superconductivity.

In this paper, we present a detailed analysis of the single-particle scattering rate in a model of the γ-band of Sr_2RuO_4. The analysis is based on a model for the strain dependence of the electronic structure that has previously been used to successfully describe both the elastocaloric effect [21] and the softening of Young's modulus [27]. We then perform a perturbative calculation of the scattering rate up to second-order in a local effective Hubbard interaction U, recovering the expected universal low-temperature behavior discussed above. Our results further demonstrate that the temperatures and energies at which the ARPES measurements of Ref. [36] were performed do not yet correspond to this universal low-energy, low-temperature regime. In particular, the apparent exponent $\alpha \approx 1.4(2)$ can be understood within our framework as arising from a combination of a quadratic Fermi-liquid contribution and the hitherto elusive linear behavior associated with the VHS,

$$\tau^{-1} = A\omega + B\omega^2. \tag{2}$$

As it is hard to determine logarithmic effects in the numerical analysis, we do not distinguish between ω, $\omega \log \omega$, or $\omega/\log \omega$. The same is true for the T-dependence of the scattering rate. These logarithmic effects are, however, discussed in Appendix in more detail, where we also comment on the fact that the quantitative importance of the logarithmic corrections are rather small.

Likewise, we find that, in the temperature and frequency range relevant to Ref. [36], the $\omega^{3/2}$ dependence of the scattering rate for states away from the Van Hove point is significantly affected by ω^2 corrections. This follows from the comparatively small phase space available for processes giving rise to a $\omega^{3/2}$ rate. Our analysis thus explains the puzzling observations of Ref. [36] and may also aid in the interpretation of other probes of the anisotropic scattering rate, such as electronic Raman scattering. In addition, we expect a $T^{3/2}$ dependence of the scattering rate in thermal transport, and hence a thermal conductivity scaling as $\kappa(T) \sim T^{-1/2}$, only for $T < 10$ K.

II. THE MODEL

We focus our analysis on the role of the γ-band of Sr_2RuO_4 (Fermi surface sheet in Fig. 1 marked in color) that is dominated by Ru-4d_{xy} states. We note that there are two additional Fermi surface sheets (marked by dashed lines in Fig. 1), referred to as the α- and β-sheets, that are predominantly made up of coupled Ru-4d_{xz} and -4d_{yz} orbitals. The contribution of the α- and β-sheets to the overall density of states is comparatively small [41,50]. More importantly, it is the γ-sheet where the Fermi energy crosses the VHS upon applying uniaxial stress. A discussion of the role of the α- and β-sheets for the kinematics of scattering processes in the electrical resistivity can be found in Ref. [22]. For the remaining γ-band, we use

the Hubbard model,

$$H = \sum_{\boldsymbol{k},\sigma} \varepsilon_{\boldsymbol{k}} c^{\dagger}_{\boldsymbol{k}\sigma} c_{\boldsymbol{k}\sigma} + U \sum_{i} n_{i\uparrow} n_{i\downarrow}, \tag{3}$$

where the strain-dependent electronic dispersion has the form [21,27]

$$\begin{aligned}\varepsilon(\boldsymbol{k}) = &-2t_x \cos(k_x) - 2t_y \cos(k_y) \\ &- 4t' \cos(k_x)\cos(k_y) - \mu\end{aligned} \tag{4}$$

with hopping parameters $t_x = t_0(1-\alpha\epsilon)$, $t_y = t_0(1+\alpha\nu_{xy}\epsilon)$, $t' = t'_0[1-\alpha/2(1-\nu_{xy})\epsilon]$, and $\mu = 1.48t_0$, and where the numerical values are taken as $\alpha = 7.604$, $t_0 = 0.119$ eV, $t'_0 = 0.392t_0$, and with Poisson ratio $\nu_{xy} \approx 0.51$, obtained from the elastic constants from Ref. [51]. The uniaxial strain parameter $\epsilon = \partial_x u_x$ with displacement vector $\boldsymbol{u}$ controls the degree of anisotropy of the Fermi surface, and tunes a single Van Hove point to the Fermi surface at the critical strain value $\epsilon_{\mathrm{VH}} \approx -0.44\%$. This is very close to the value at which the Lifshitz transition was observed experimentally in Sr_2RuO_4 [52,53]. The tight-binding parametrization of Eq. (4) follows from fits to ARPES results of Ref. [54] at zero strain, $\epsilon = 0$, and led to excellent quantitative agreement for the strain dependence of the elastocaloric effect and Young's modulus [21,27]. Effects due to the dispersion along the c-direction are small, particularly near the Van Hove point, where three-dimensional effects are only relevant below $2-4$ K [41,55].

The retarded single-particle self-energy at second-order in U and at finite temperature T is expressed as

$$\Sigma_{\boldsymbol{k}}(\omega, T) = -U^2 \int \frac{d^2\boldsymbol{q}}{(2\pi)^2} \frac{d^2\boldsymbol{k}_1}{(2\pi)^2} \frac{\left[n_F(\varepsilon_{\boldsymbol{k}_1}) - n_F(\varepsilon_{\boldsymbol{k}_1+\boldsymbol{q}})\right]\left[n_B(\varepsilon_{\boldsymbol{k}_1+\boldsymbol{q}} - \varepsilon_{\boldsymbol{k}_1}) + n_F(-\varepsilon_{\boldsymbol{k}-\boldsymbol{q}})\right]}{\varepsilon_{\boldsymbol{k}_1+\boldsymbol{q}} - \varepsilon_{\boldsymbol{k}_1} + \varepsilon_{\boldsymbol{k}-\boldsymbol{q}} - \omega - i0^+}, \tag{5}$$

where n_F and n_B are the Fermi and Bose functions, respectively, and the integration is over the first Brillouin zone. From this, the quasiparticle scattering rate $\tau^{-1}_{\boldsymbol{k}}(\omega, T)$ is extracted via

$$\tau^{-1}_{\boldsymbol{k}}(\omega, T) = -2Z_{\boldsymbol{k}}(T)\mathrm{Im}\Sigma_{\boldsymbol{k}}(\omega, T), \tag{6}$$

where the quasiparticle weight is defined as

$$Z_{\boldsymbol{k}}(T) = \left(1 - \frac{\partial\, \mathrm{Re}\,\Sigma_{\boldsymbol{k}}(\omega, T)}{\partial\omega}\bigg|_{\omega=0}\right)^{-1}. \tag{7}$$

We will also use the notation

$$\Gamma_{\boldsymbol{k}}(\omega, T) = -\mathrm{Im}\Sigma_{\boldsymbol{k}}(\omega, T). \tag{8}$$

Note that the frequency dependence of the scattering rate is determined entirely by $\Gamma_{\boldsymbol{k}}(\omega, T)$, while the temperature and momentum dependence are also determined by $Z_{\boldsymbol{k}}(T)$. In what follows, we will primarily focus on $\Gamma_{\boldsymbol{k}}(\omega, T)/U^2$ as it does not rely on knowledge of the value of the effective interaction U. In Eq. (10) below, we will also comment on the quasiparticle weight and the scattering rate $\tau^{-1}_{\boldsymbol{k}}(\omega, T)$.

Before presenting the numerical results for the self-energy, we comment on the appropriateness of employing second-order perturbation theory. Sr_2RuO_4 is a correlated material with complex interactions that couple spin, charge, and orbital excitations at high energies [56,57]. Numerical renormalization-group calculations [58] show that, at low energies $T < T_{\mathrm{FL}}$, these orbital excitations are strongly screened, explaining the observed emergence of a good Fermi liquid; see Ref. [41]. Our analysis is therefore meaningful in this low-energy, low-temperature regime, where such screening has taken place and the phase-space arguments of Fermi-liquid theory apply. In this regime, second-order perturbation theory is expected to provide the dominant contribution to the scattering rate, provided the system does not develop an instability towards an ordered state. Higher-order processes are then expected to renormalize the overall coefficient in the scattering rate without significantly altering its frequency or temperature dependence. An analysis based on the random phase approximation is expected to provide exactly the same qualitative results. In this sense, the interaction parameter U of our analysis should be viewed as an effective interaction, analogous to a Landau parameter. Below, we briefly comment on the appropriate choice of U. Hence, the exponents—which constitute the main result of our analysis—are expected to be reliably captured by second-order perturbation theory. However, this approach is not anticipated to yield a quantitatively accurate value for the numerical prefactor of the scattering rate. A similar situation arises in a Hund's metal: although it represents an exotic state of matter at higher energies, its low-energy behavior ultimately crosses over to that of a Fermi liquid. Furthermore, at the lowest energies, some instability is expected. For a discussion of the superconducting instability in systems with a single Van Hove point, see Ref. [13]. Reference [13] also performed a two-loop analysis for a single Van Hove point, yielding the characteristic temperature scale $k_{\mathrm{B}}T^* \approx t\exp(-\frac{4\pi^2 t}{bU})$ with $b = 1.88$ and t the nearest-neighbor hopping element. For $T < T^*$, our perturbative treatment must break down because of the divergent density of states at the Fermi level. Even for $U \sim t$, this scale is exceedingly small compared to t. In praxis, the onset of superconductivity seems more relevant in real systems than the energy scale T^*. We will consider the regime above the onset of superconductivity but still low in energy.

III. NUMERICAL RESULTS

A. Anisotropy of the scattering rate

Before we discuss the frequency and temperature dependences of the scattering rate, we briefly show the anisotropy of $\Gamma_{\boldsymbol{k}}(\omega = 0, T)$ at low T along the Fermi surface (Fermi line). Figure 2 illustrates the momentum dependence of the zero-frequency scattering rate along the Fermi surface, both at zero strain and at the Lifshitz transition. At zero strain (light-blue curve), $\Gamma_{\boldsymbol{k}}$ exhibits only a moderate angular variation: although the Fermi surface is already anisotropic, no special points dominate the phase space for small-momentum particle-hole excitations. Consequently, the scattering rate remains of comparable magnitude around the entire Fermi contour.

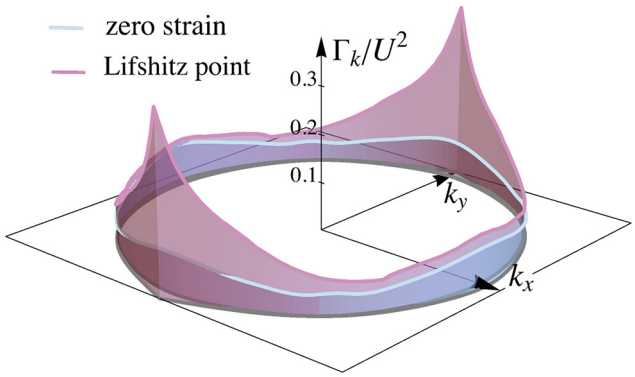

FIG. 2. Anisotropy of the zero-frequency scattering rate Γ_{k_F}/U^2 on the Fermi surface at $T = 9.9$ K for zero strain (light blue) and the critical strain of the Lifshitz transition (pink). The base area marks the first Brillouin zone boundary, and Γ_{k_F}/U^2 is measured in units of 10^{-2} eV^{-1}. While the scattering rate at zero strain is moderately anisotropic, a pronounced anisotropy with a sharp peak at the Van Hove point emerges at the Lifshitz transition.

In contrast, at the Lifshitz transition (pink curve), the anisotropy becomes dramatically enhanced. A sharp and narrow peak develops at the Van Hove momenta ($\phi = 0$ and symmetry-related points), reflecting the large phase space for scattering off the broad continuum of compressive particle-hole excitations described by Eq. (1). As a result, quasiparticles at the Van Hove point—our "hot" states—experience a scattering rate that is significantly larger than elsewhere on the Fermi surface. Away from the VHS (e.g., near $\phi = \pi/4$ or $\pi/2$, etc.), the scattering rate remains much smaller. These "cold" regions feel only the reduced phase space associated with conventional processes involving finite curvature of the Fermi surface. The result is the pronounced hot-cold dichotomy familiar from systems tuned to a single two-dimensional VHS.

The strong enhancement of $\Gamma_{\boldsymbol{k}}$ near the Van Hove point is closely related to the distinct frequency and temperature dependence discussed later in this section: linear-in-T scattering of hot carriers and $T^{3/2}$ behavior in cold regions. Moreover, the sharp anisotropy shown in Fig. 2 provides a direct spectroscopic signature of approaching the Lifshitz transition and is consistent with the strong strain dependence inferred from the ARPES measurements of Ref. [36].

B. Temperature dependence of Γ

The temperature dependence of the imaginary part of the self-energy at zero frequency, $\Gamma_{\boldsymbol{k}}(\omega = 0, T)$, is shown both at zero strain and at the strain value of the Lifshitz transition in the top and bottom panel of Fig. 3, respectively. At zero strain, the Fermi surface has no special features, leading to the canonical Fermi liquid dependence $\Gamma \sim T^2$ at the lowest temperatures at all points on the Fermi surface. For the single-particle self-energy, one further expects additional logarithmic corrections to the T^2 behavior due to collinear scattering [59–61]. As this regime is not of our primary concern, we have not attempted to analyze the quantitative magnitude of these corrections. In contrast, at the critical strain, the self-energy acquires a substantial momentum dependence, and it exhibits

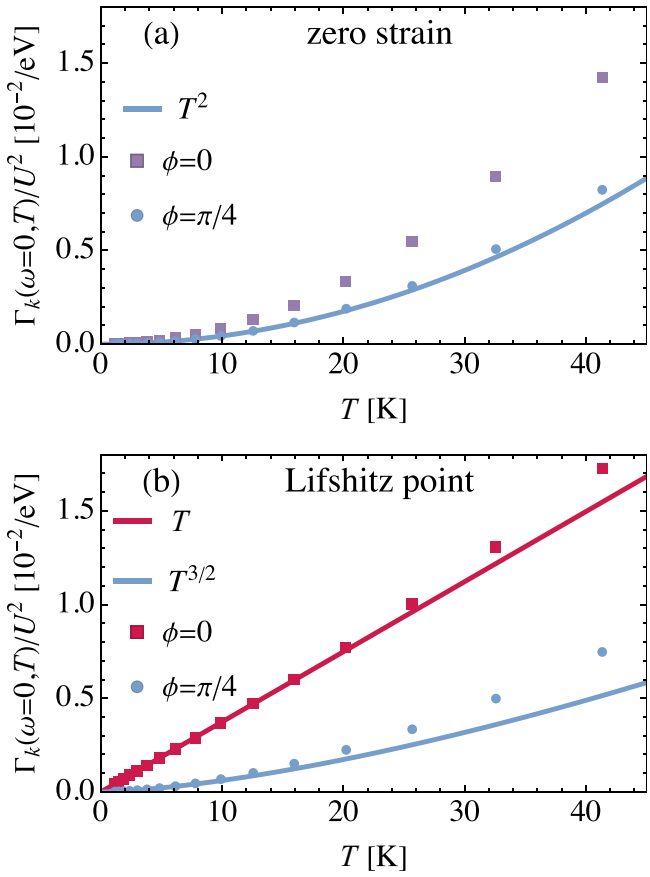

FIG. 3. Temperature dependence of the imaginary part of the zero-frequency self-energy, $\Gamma_{\boldsymbol{k}}(0, T)$, for cold and hot momenta on the Fermi surface: $\phi = 0$ corresponds to the Van Hove point while $\phi = \pi/4$ is away from it. (a) Zero strain displaying low-T quadratic Fermi liquid behavior with all states being cold. (b) Critical strain exhibiting T-linear behavior at $\phi = 0$ (hot) and $T^{3/2}$ behavior away from the Van Hove point with $\phi = \pi/4$ (cold).

anomalous $\Gamma \sim T$ scalings with temperature at the Van Hove point and $\Gamma \sim T^{3/2}$ away from it. While a slightly better fit to the data can be achieved with an additional term $\sim T \log(D/T)$ included, the distinction is hardly visible and will not be included in our subsequent discussion. As discussed earlier, these exponents arise from scattering involving the particle-hole excitations of Eq. (1) [22,31–35]. For cold parts of the Fermi surface (marked in blue in Fig. 1), the dominant processes giving rise to these power laws are scattering events where a pair of cold and hot momentum states scatter into another pair of cold and hot momentum states. We refer to these processes as ch → ch. On the other hand, for the hot parts of the Fermi surface located near the Van Hove point (marked in red in Fig. 1), the scattering rate is caused by a pair of hot momentum states scattering into a second pair of hot states. We refer to these events as hh → hh. Below we will analyze these distinct contributions in detail.

C. Frequency dependence of Γ

For a more direct comparison with the experiment of Ref. [36], which reports the scattering rate at constant temperature $T = 11$ K at the Lifshitz transition, we now

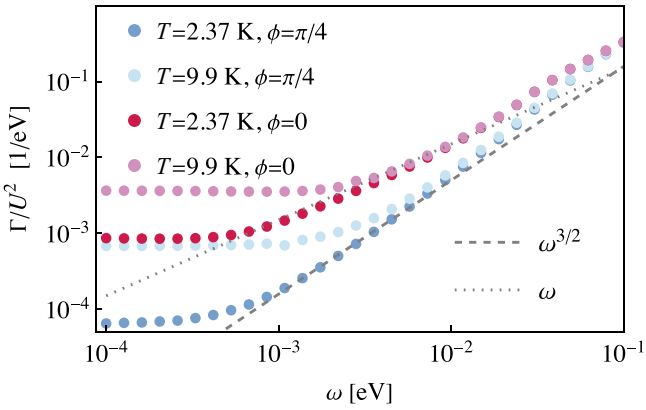

FIG. 4. Log-log plot of the frequency dependence of the imaginary part of the self-energy at the critical strain.

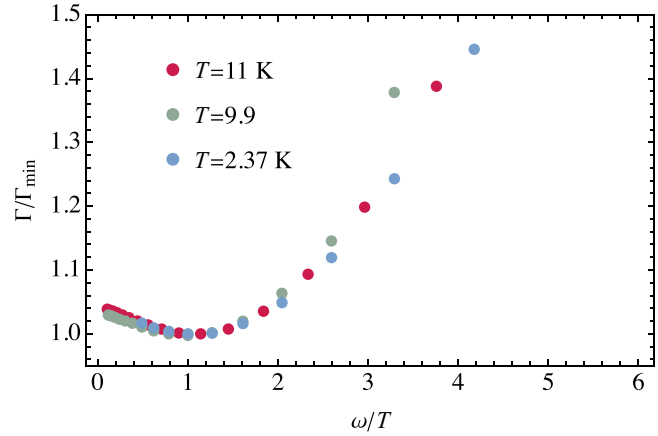

FIG. 5. Scattering rate Γ at the Lifshitz point and for the momentum at the Van Hove point as a function of frequency for different temperatures. To facilitate the comparison of different T, Γ has been scaled by the value at the local minimum and is plotted as a function of ω/T. The physical origin of the nonmonotonic dependence of the scattering rate is further discussed in Appendix.

turn to the frequency dependence of Γ. The imaginary-part of the self-energy as a function of frequency is shown in Fig. 4 for two different temperatures $T = 2.37$ and 9.9 K. At $T = 2.37$ K and within the low-energy window 10^{-3} eV–10^{-2} eV, we observe the same scaling exponents seen in the temperature dependence in Fig. 3. Meanwhile, at even lower energies $\omega < 10^{-3}$ eV, we enter the frequency-independent regime, where Γ depends weakly on frequency but strongly on temperature. On the other hand, at the higher temperature, the expected exponents are not present in any appreciable energy-window due to the onset of the frequency-independent regime at a higher-energy scale, before the universal low-energy regime is reached. Instead, at a temperature $T = 9.9$ K and at the Van Hove point ($\phi = 0$), we find an apparent power-law scaling with a larger exponent of approximately 3/2 between energies of order 10^{-2} and 10^{-1} eV. This is the same power-law behavior seen in the ARPES experiment, which obtained an exponent 1.4(2) by fitting the ARPES data in the frequency range [–50,10] meV, which is roughly the same range in which we observe this apparent exponent. In Fig. 5 we also show the frequency dependence at the Van Hove point on a linear scale. Remarkably, at finite temperature, the scattering rate $\Gamma_{\boldsymbol{k}}(\omega, T)$ at the Van Hove point displays a nonmonotonic frequency dependence, highlighting the unusual single-particle dynamics at a Lifshitz point. In Appendix, we demonstrate that the scattering rate attains a minimum at $\omega \sim T$, arising from the competing effects of thermal and quantum excitations of the compressive mode described by Eq. (1). At $T = 0$, the scattering rate rises, as expected, monotonic with ω.

D. Origin of the apparent high-frequency exponent

To understand the origin of the putative high-frequency power law, we can analyze the role of the different scattering processes involving hot states near and cold states away from the Van Hove point individually. Since we are considering a single connected Fermi surface, the boundary between the hot and cold regions is somewhat arbitrary: our choice is shown in Fig. 1. Specifically, the hot region is defined as the rectangular region of the Brillouin zone with corners on the Fermi surface, over which the average magnitude of the dispersion differs by at most a tolerance of 15% from that of the Van Hove dispersion Taylor-expanded around $(0, \pi)$. We note that we checked explicitly that our results do not depend on reasonable changes to the tolerance. Concentrating on the behavior at the Van Hove point, there are several contributions to the scattering rate: (i) hh → hh processes that are dominant at low T and yield $\Gamma \sim T$. (ii) ch → ch processes that are associated with a small transferred momentum yet come with a large phase space. These events yield $\Gamma \sim T^2$. (iii) hh → ch processes that have a rather small phase space since, with the exception of the states close to the boundary between the hot and cold regions, these events require the transferred momentum to be small (h → h) and large (h → c) at the same time. (iv) ch → cc events that also come with a small phase space, yet play a role in the electrical resistivity as the momentum transfer is large. Notice, since we are considering the self-energy at the Van Hove point, we always have at least one hot state.

The decomposition of the second-order self-energy into these different contributions is achieved as follows. We rewrite the Green's function as

$$G_{\boldsymbol{k}} = G_{h,\boldsymbol{k}} + G_{c,\boldsymbol{k}} = \theta_h(\boldsymbol{k}) G_{\boldsymbol{k}} + \theta_c(\boldsymbol{k}) G_{\boldsymbol{k}}, \tag{9}$$

where the support functions $\theta_h(\boldsymbol{k})$ [$\theta_c(\boldsymbol{k})$] are unity for momenta $\boldsymbol{k}$ in the hot (cold) regions of the Brillouin zone, and zero otherwise. The three internal Green's functions in the self-energy diagram can each be either hot or cold: these possibilities comprise the four channels listed above. For instance, all three Green's function in the hh → hh contribution are hot, while the ch → ch is the sum of the three contributions with a single internal G_h.

The self-energies arising from only hh → hh as well as ch → ch processes are shown in Fig. 6. We see that hh → hh events are dominant at low temperatures and give a linear-in-temperature scaling, while the contribution from ch → ch scattering scales with temperature quadratically and thus becomes sizable at higher T. Remarkably, the sum of these two contributions agrees perfectly with the full self-energy

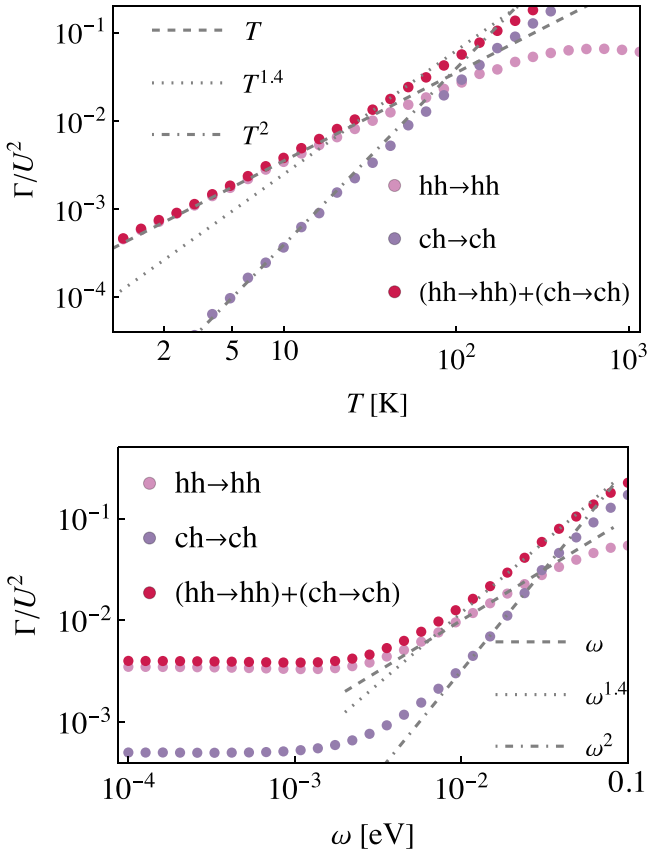

FIG. 6. Contributions to the scattering rate as a function of temperature for $\omega = 0$ (upper panel) and frequency for $T = 11$ K (lower panel) at the Van Hove momentum and at the Lifshitz transition. We show contributions due to hh → hh and ch → ch scattering processes; their sum (shown in red) is indistinguishable from the total scattering rate (not shown). At very low frequencies, hh → hh processes dominate and yield a linear behavior; in the intermediate regime, ch → ch processes become comparable and behave like T^2 or ω^2. No pure power-law behavior occurs. The sum of different contributions may only appear as a power law with an intermediate exponent.

(not shown in Fig. 6) that includes all possible scattering processes. Hence, these two processes are dominant, and all others can be neglected. This analysis shows in detail how the putative intermediate exponent $\alpha = 1.4(2)$ seen in Ref. [36] results from the crossover between the T and T^2 scalings. We also note that the nonmonotonic frequency dependence of the scattering rate, discussed in the previous subsection and in Appendix, only occurs for hh → hh processes and is absent in the ch → ch channel.

The experiment of Ref. [36] finds $\tau_{\text{exp}}^{-1} = 4 \pm 1$ meV for the scattering rate of Eq. (6) at the Lifshitz point, for $T = 11$ K, and at a frequency $\omega = -5$ meV. For the same parameters, we find $-\text{Im}\Sigma(-5\ \text{meV}) = 8.0(2)\tilde{U}^2$ meV and $\partial_\omega \text{Re}\Sigma|_{\omega=0} = -6.1(2)\tilde{U}^2$, where $U = \tilde{U}$ eV defines the dimensionless interaction strength $\tilde{U}$. Hence within second-order perturbation theory, we could choose a value of U such that

$$\tau_{\text{exp}}^{-1} = \frac{16\tilde{U}^2}{1 + 6.1\tilde{U}^2}\ \text{meV}. \tag{10}$$

For $\tilde{U} \sim 1$ this gives the correct order of magnitude $\tau_{\text{exp}}^{-1} \sim 2.25$ meV, yet $\tilde{U} \sim 1$ with a bandwidth of order 1 eV is clearly beyond the regime where we can reliably use second-order perturbation theory. As discussed earlier, while we expect the power laws in frequency and temperature to be appropriately reproduced, the precise magnitude of the scattering rate is beyond the accuracy of the second-order perturbation theory. This can already be seen from the fact that $\tau_{\text{exp}}^{-1} = 4$ meV cannot be reproduced for any value of $\tilde{U}$, clearly an indication that higher-order processes will change the $\tilde{U}$-dependence in Eq. (10). It is precisely the fact that this estimate yields the correct order of magnitude that seems to suggest that our approach reasonably describes the dominant scattering events of the material in the low-T regime.

IV. CONCLUSIONS

We presented a detailed theoretical analysis of the quasiparticle scattering rate in the γ-band of strained Sr_2RuO_4 in the vicinity of the uniaxial-strain-induced Lifshitz transition. Based on a realistic tight-binding model and second-order perturbation theory in an effective local interaction, we find at the Lifshitz point a strong anisotropy of the scattering rate in momentum space, and we confirm the universal low-energy behavior associated with a single VHS [22,31,32]: at the hot spots, the scattering rate varies linearly in frequency or temperature, while away from these points we recover the expected $\omega^{3/2}$ or $T^{3/2}$ scaling.

Our results provide a natural explanation for the apparent non-Fermi-liquid exponent $\alpha \approx 1.4(2)$ observed in recent ARPES experiments [36]. We find strong evidence that this intermediate-energy behavior does not reflect new universal physics, but instead arises from a crossover regime in which the linear-in-ω scattering of hot quasiparticles near the Van Hove point and the quadratic Fermi-liquid-like scattering, involving both hot and cold regions of the Fermi surface, are of comparable magnitude. This competition leads to the effective intermediate exponent reported in Ref. [36]. Nevertheless, the overall energy dependence observed experimentally strongly suggests that, sufficiently close to the Lifshitz critical point, the true low-energy behavior is governed by a linear-in-energy scattering rate.

For states away from the Van Hove point, we find that the comparatively narrow phase space for processes giving rise to the $\omega^{3/2}$ behavior restricts its observability to temperatures below ≈10 K or energies below 10 meV. In particular, we expect the emergence of a thermal conductivity scaling $\kappa \sim T^{-1/2}$, discussed in Ref. [22], only for $T \lesssim 10$ K. These results indicate that, aside from the resistivity measurements of Ref. [20], current experiments have not yet accessed the true universal low-energy regime where collision rates are controlled by the VHS and the associated Lifshitz transition. Our work, therefore, provides quantitative predictions for the strong anisotropy and strain dependence of the scattering rate that can be tested in future spectroscopic and thermal-transport studies.

A further outcome of our analysis is the identification of scattering off the broad continuum of compressive particle-hole excitations described by Eq. (1) as the dominant

low-energy scattering mechanism near the Lifshitz transition. These same excitations are responsible for both the pronounced lattice softening [27] and the enhanced normal-state entropy [21] observed experimentally at the transition, highlighting a common origin of the associated anomalies.

With regard to the superconducting state, the entropy maximum as a function of strain in the normal state is replaced by a minimum below T_c [21], which has been interpreted as strong evidence that electronic states near the Van Hove point become gapped below T_c [62]. At the very least, this implies that the compressive particle-hole excitations described by Eq. (1) must be included in any analysis of the pairing mechanism in Sr_2RuO_4 [63].

ACKNOWLEDGMENTS

We are grateful to F. Baumberger, E. Berg, F. Henssler, A. Hunter, M. Le Tacon, A. P. Mackenzie, P. H. McGuinness, G. Palle, B. J. Ramshaw, and A. Tamai for helpful discussions. This work was supported by the UK Engineering and Physical Sciences Research Council through Grants No. EP/X012557/1 (D.T.S.P. and J.J.B.), No. EP/X01245X/1 (B.C. and E.K.), and the German Research Foundation (DFG) through CRC TRR 288 "Elasto-Q-Mat," Project No. A07 (J.S.). The calculations were performed using King's Computational Research, Engineering and Technology Environment (CREATE).

DATA AVAILABILITY

The data that support the findings of this article are openly available [64].

APPENDIX: ON THE NONMONOTONIC hh → hh SCATTERING

In the main text, we presented the curious result that the scattering rate $\Gamma_{\boldsymbol{k}}(\omega, T)$ at the Lifshitz transition and for $\boldsymbol{k}$ at the Van Hove point is, at finite T, a nonmonotonic function of frequency ω. Here we confirm this finding using an analytical approach. This analysis shows that the minimum of the scattering rate occurs for $\omega \sim T$ and is a result of competing tendencies of thermal and quantum excitations of the compressive mode described by Eq. (1).

For the analysis of hh → hh processes, we can focus on the states in the vicinity of the Van Hove point and use the dispersion

$$\varepsilon_{\boldsymbol{k}} = \frac{1}{2m}\left(k_x^2 - k_y^2\right). \tag{A1}$$

The corresponding electronic density of states is $\rho(\epsilon) = \frac{m}{\pi^2}\log(D/|\epsilon|)$. $\sqrt{mD}$ is the typical momentum scale where the above expansion is valid, i.e., approximately the region marked in red in Fig. 1. At finite T, the spectrum $\mathrm{Im}\Pi(\boldsymbol{q}, \omega)$ of compressive modes can be described by Eq. (1) with $\varepsilon_{\mathrm{VH}}(\boldsymbol{q})$ replaced by $\sqrt{\varepsilon_{\mathrm{VH}}(\boldsymbol{q})^2 + T^2}$ [22]. We further note that with Eq. (1), the momentum dependence of $\mathrm{Im}\Pi(\boldsymbol{q}, \omega)$ only enters through $\varepsilon_{\mathrm{VH}}(\boldsymbol{q})$, which we indicate by

$$\mathrm{Im}\Pi(\boldsymbol{q}, \omega) = \mathrm{Im}\Pi(\varepsilon_{\mathrm{VH}}(\boldsymbol{q}), \omega). \tag{A2}$$

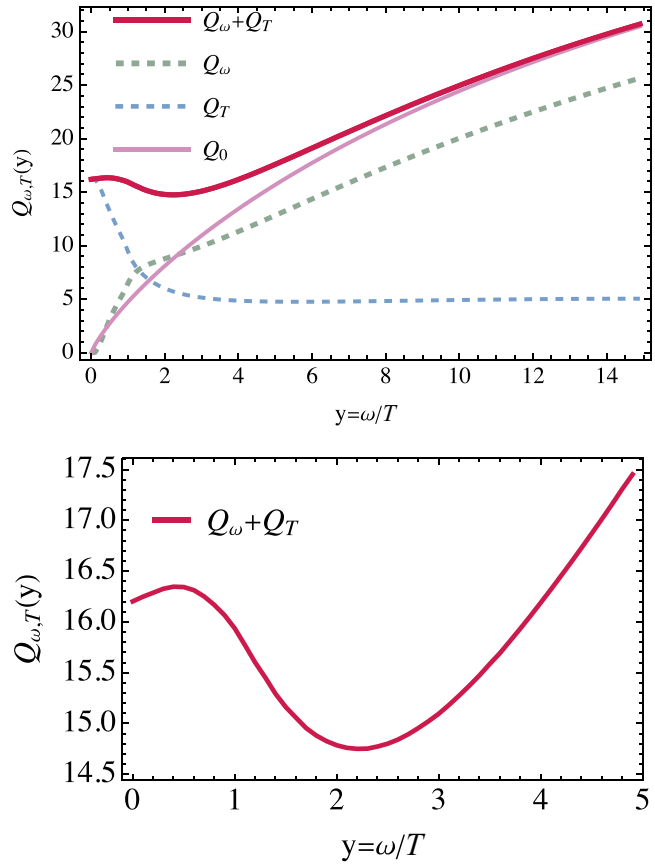

FIG. 7. Quantum Q_ω and thermal Q_T contributions to the scattering rate Eq. (A8) as a function of ω/T along with their sum and in comparison with the zero-temperature contribution that follows from Eq. (A5). The lower panel shows $Q_\omega + Q_T$ near the minimum at $\omega \approx 2.25T$. The minimum is a consequence of the rapid drop in Q_T for energies comparable to T.

The scattering rate right at the Van Hove point,

$$\Gamma_{\mathrm{VH}}(\omega, T) = \Gamma_{\boldsymbol{k}}(\omega, T), \tag{A3}$$

can then be written as an integral over energy only:

$$\Gamma_{\mathrm{VH}}(\omega, T) = 2U^2 \int d\epsilon \rho(\epsilon) S(\epsilon, \omega) \mathrm{Im}\Pi(\epsilon, \omega - \epsilon), \tag{A4}$$

with $S(\epsilon, \omega) = n_F(\epsilon) + n_B(\epsilon - \omega)$.

We first consider the limit $T = 0$. Then we obtain

$$\Gamma_{\mathrm{VH}}(\omega, 0) = \frac{U^2 m}{\pi}\left(\int_0^{\omega/2} d\epsilon \rho(\varepsilon) + \int_{\omega/2}^{\omega} d\epsilon \rho(\varepsilon)\frac{\omega - \epsilon}{\epsilon}\right)$$
$$= \lambda\omega\left(1 + \log\frac{\sqrt{2}D}{\omega}\right), \tag{A5}$$

with dimensionless coupling constant $\lambda = m^2U^2 \log 2/\pi^3$. In the opposite limit of $\omega = 0$ but finite T, we obtain instead

$$\Gamma_{\mathrm{VH}}(0, T) = \frac{2U^2m^2}{\pi^3} T \int_0^{D/T} dx \frac{\log\frac{D}{xT}}{\sinh(x)} \frac{x}{\sqrt{x^2+1}}$$
$$= \frac{2\lambda}{\log 2} T\left(c + c' \log\frac{D}{T}\right), \tag{A6}$$

with $c = 0.5338$ and $c' = 1.497\,26$. The integrals over x have been numerically evaluated with the upper limit $D/T \to \infty$.

Finally, we consider the case with generic ω/T:

$$\Gamma_{\mathrm{VH}}(\omega, T) = -\frac{U^2 m^2}{\pi^3}\int_{\epsilon^*}^{D} d\epsilon \log\left(\frac{D}{|\epsilon|}\right)\frac{S(\epsilon,\omega)(\omega-\epsilon)}{\sqrt{\epsilon^2+T^2}} - \frac{U^2 m^2}{\pi^3}\int_{-D}^{\epsilon^*} d\epsilon \log\left(\frac{D}{|\epsilon|}\right) S(\epsilon,\omega), \tag{A7}$$

where $\epsilon^* = \frac{\omega^2 - T^2}{2\omega}$. This can be written as

$$\Gamma_{\mathrm{VH}}(\omega, T) = \lambda T\left[Q_\omega\left(\frac{\omega}{T}\right) + Q_T\left(\frac{\omega}{T}\right)\right] \tag{A8}$$

with

$$Q_\omega(y) = -\int_{-d}^{x^*(y)} \frac{dx \log\left(\frac{d}{|x|}\right)}{\log 2} s(x,y),$$
$$Q_T(y) = -\int_{x^*(y)}^{d} \frac{dx \log\left(\frac{d}{|x|}\right)}{\log 2} \frac{s(x,y)(y-x)}{\sqrt{x^2+1}}. \tag{A9}$$

Here, $x^*(y) = \frac{y^2-1}{2y}$ and $s(x,y) = \frac{1}{e^x+1} + \frac{1}{e^{x-y}-1}$. Notice, Q_ω and Q_T also depend on the ratio of the upper-energy cutoff and temperature: $d \equiv D/T$. Except for the argument of the logarithm, this dependency is weak and hence suppressed. The zero-temperature rate of Eq. (A5) can be written as $Q_0(y) = y(1 + \log\frac{\sqrt{2}d}{y})$, while $Q(0) = \frac{2}{\log 2}(c + c' \log d)$ corresponds to Eq. (A6).

Q_ω is the *quantum contribution* to the scattering rate and is caused by compressive excitations with energies larger than T, while conversely Q_T is, except for an overall constant, dominated by the corresponding *thermal contribution*. In Fig. 7 we show the $y = \omega/T$ dependence of $Q_\omega(y)$, $Q_T(y)$ (dashed lines), and their sum (solid red line) in comparison with the $T = 0$ result $Q_0(y)$ (pink solid line) at large $d = 30$. Q_ω dominates at $\omega \gg T$ and gives rise to the $\omega \log \omega$ dependence of the scattering rate. Only Q_T contributes at $\omega = 0$. It approaches a constant at large y. For small but finite argument, the y-dependence of the two contributions is opposite and almost cancels to a constant. However, for $\omega \sim T$ the thermal contribution to the rate, governed by Q_T, drops faster than the quantum contribution Q_ω rises. This is the reason for the local minimum of the scattering rate at $\omega \approx 2.25T$.

Finally, we comment on the detailed role of logarithmic corrections to the scattering rate Γ and the inverse lifetime τ^{-1}. At the VHS, the dominant low-energy contribution to the imaginary part of the self-energy is $\mathrm{Im}\Sigma(\omega) = -\lambda|\omega| \log\frac{D}{|\omega|}$; see Eq. (A5). Kramers-Kronig transforming this result yields for the real part $\mathrm{Re}\Sigma(\omega) = -\frac{\lambda\omega}{\pi}\log^2\frac{D}{|\omega|}$. Hence the quasiparticle residue of Eq. (7) for small ω behaves as $Z(\omega) = \frac{\pi}{\lambda \log^2\frac{D}{\omega}}$. Hence, we obtain the following for the inverse lifetime of Eq. (6): $\tau^{-1}(\omega) = 2\pi|\omega|/\log\frac{\Lambda}{\omega}$. We note that the logarithmic contribution to the self-energy is a direct consequence of the logarithmic divergence of the density of states at the VH point. If a constant background were included in the density of states, the relative magnitude of the coefficient of the logarithmic terms would be reduced, which explains why they are harder to observe in the numerical analysis of the tight-binding dispersion presented in the main text.

[1] L. Van Hove, The occurrence of singularities in the elastic frequency distribution of a crystal, Phys. Rev. **89**, 1189 (1953).

[2] L. Classen and J. J. Betouras, High-order Van Hove singularities and their connection to flat bands, Ann. Rev. Condens. Matter **16**, 229 (2025).

[3] J. L. McChesney, A. Bostwick, T. Ohta, T. Seyller, K. Horn, J. González, and E. Rotenberg, Extended van Hove singularity and superconducting instability in doped graphene, Phys. Rev. Lett. **104**, 136803 (2010).

[4] R. Nandkishore, L. S. Levitov, and A. V. Chubukov, Chiral superconductivity from repulsive interactions in doped graphene, Nat. Phys. **8**, 158 (2012).

[5] M. L. Kiesel, C. Platt, W. Hanke, D. A. Abanin, and R. Thomale, Competing many-body instabilities and unconventional superconductivity in graphene, Phys. Rev. B **86**, 020507(R) (2012).

[6] W.-S. Wang, Y.-Y. Xiang, Q.-H. Wang, F. Wang, F. Yang, and D.-H. Lee, Functional renormalization group and variational Monte Carlo studies of the electronic instabilities in graphene near $\frac{1}{4}$ doping, Phys. Rev. B **85**, 035414 (2012).

[7] A. M. Black-Schaffer and C. Honerkamp, Chiral d-wave superconductivity in doped graphene, J. Phys.: Condens. Matter **26**, 423201 (2014).

[8] A. Shtyk, G. Goldstein, and C. Chamon, Electrons at the monkey saddle: A multicritical Lifshitz point, Phys. Rev. B **95**, 035137 (2017).

[9] N. F. Yuan, H. Isobe, and L. Fu, Magic of high-order van Hove singularity, Nat. Commun. **10**, 5769 (2019).

[10] H. Isobe and L. Fu, Supermetal, Phys. Rev. Res. **1**, 033206 (2019).

[11] N. F. Q. Yuan and L. Fu, Classification of critical points in energy bands based on topology, scaling, and symmetry, Phys. Rev. B **101**, 125120 (2020).

[12] A. Chandrasekaran, A. Shtyk, J. J. Betouras, and C. Chamon, Catastrophe theory classification of Fermi surface topological transitions in two dimensions, Phys. Rev. Res. **2**, 013355 (2020).

[13] R. Ojajärvi, A. V. Chubukov, Y.-C. Lee, M. Garst, and J. Schmalian, Pairing at a single Van Hove point, npj Quantum Mater. **9**, 105 (2024).

[14] Y. Hu, X. Wu, B. R. Ortiz, S. Ju, X. Han, J. Ma, N. C. Plumb, M. Radovic, R. Thomale, S. D. Wilson, *et al.*, Rich nature of Van Hove singularities in Kagome superconductor CsV_3Sb_5, Nat. Commun. **13**, 2220 (2022).

[15] M. L. Kiesel and R. Thomale, Sublattice interference in the kagome Hubbard model, Phys. Rev. B **86**, 121105(R) (2012).

[16] T. Park, M. Ye, and L. Balents, Electronic instabilities of kagome metals: Saddle points and Landau theory, Phys. Rev. B **104**, 035142 (2021).

[17] H. Li, Y. B. Kim, and H.-Y. Kee, Intertwined Van Hove singularities as a mechanism for loop current order in kagome metals, Phys. Rev. Lett. **132**, 146501 (2024).

[18] D. V. Efremov, A. Shtyk, A. W. Rost, C. Chamon, A. P. Mackenzie, and J. J. Betouras, Multicritical Fermi surface topological transitions, Phys. Rev. Lett. **123**, 207202 (2019).

[19] C. W. Hicks, D. O. Brodsky, E. A. Yelland, A. S. Gibbs, J. A. N. Bruin, M. E. Barber, S. D. Edkins, K. Nishimura, S. Yonezawa, Y. Maeno, and A. P. Mackenzie, Strong increase of T_c of Sr_2RuO_4 under both tensile and compressive strain, Science **344**, 283 (2014).

[20] M. E. Barber, A. S. Gibbs, Y. Maeno, A. P. Mackenzie, and C. W. Hicks, Resistivity in the vicinity of a Van Hove singularity: Sr_2RuO_4 under uniaxial pressure, Phys. Rev. Lett. **120**, 076602 (2018).

[21] Y.-S. Li, M. Garst, J. Schmalian, S. Ghosh, N. Kikugawa, D. A. Sokolov, C. W. Hicks, F. Jerzembeck, M. S. Ikeda, Z. Hu, B. J. Ramshaw, A. W. Rost, M. Nicklas, and A. P. Mackenzie, Elastocaloric determination of the phase diagram of Sr_2RuO_4, Nature (London) **607**, 276 (2022).

[22] V. C. Stangier, E. Berg, and J. Schmalian, Breakdown of the Wiedemann-Franz law at the Lifshitz point of strained Sr_2RuO_4, Phys. Rev. B **105**, 115113 (2022).

[23] A. Damascelli, D. H. Lu, K. M. Shen, N. P. Armitage, F. Ronning, D. L. Feng, C. Kim, Z.-X. Shen, T. Kimura, Y. Tokura, Z. Q. Mao, and Y. Maeno, Fermi surface, surface states, and surface reconstruction in Sr_2RuO_4, Phys. Rev. Lett. **85**, 5194 (2000).

[24] A. Chandrasekaran, R. C. Luke, E. A. Morales, C. A. Marques, P. D. C. King, P. Wahl, and J. J. Betouras, On the engineering of higher-order Van Hove singularities in two dimensions, Nat. Commun. **15**, 9521 (2024).

[25] I. M. Lifshitz, Anomalies of electron characteristics of a metal in the high pressure region, Sov. Phys. JETP **11**, 1130 (1960).

[26] A. Steppke, L. Zhao, M. E. Barber, T. Scaffidi, F. Jerzembeck, H. Rosner, A. S. Gibbs, Y. Maeno, S. H. Simon, A. P. Mackenzie, and C. W. Hicks, Strong peak in T_c of Sr_2RuO_4 under uniaxial pressure, Science **355**, eaaf9398 (2017).

[27] H. M. Noad, K. Ishida, Y.-S. Li, E. Gati, V. Stangier, N. Kikugawa, D. A. Sokolov, M. Nicklas, B. Kim, I. I. Mazin, *et al.*, Giant lattice softening at a Lifshitz transition in Sr_2RuO_4, Science **382**, 447 (2023).

[28] P.-Y. Yang, H. M. L. Noad, M. E. Barber, N. Kikugawa, D. A. Sokolov, A. P. Mackenzie, and C. W. Hicks, Probing momentum-dependent scattering in uniaxially stressed Sr_2RuO_4 through the Hall effect, Phys. Rev. Lett. **131**, 036301 (2023).

[29] R. Hlubina, Effect of impurities on the transport properties in the Van Hove scenario, Phys. Rev. B **53**, 11344 (1996).

[30] C. H. Mousatov, E. Berg, and S. A. Hartnoll, Theory of the strange metal $Sr_3Ru_2O_7$, Proc. Natl. Acad. Sci. USA **117**, 2852 (2020).

[31] S. Gopalan, O. Gunnarsson, and O. K. Andersen, Effects of saddle-point singularities on the electron lifetime, Phys. Rev. B **46**, 11798 (1992).

[32] P. C. Pattnaik, C. L. Kane, D. M. Newns, and C. C. Tsuei, Evidence for the van Hove scenario in high-temperature superconductivity from quasiparticle-lifetime broadening, Phys. Rev. B **45**, 5714 (1992).

[33] I. Dzyaloshinskii, Extended Van-Hove singularity and related non-Fermi liquids, J. Phys. I **6**, 119 (1996).

[34] D. Menashe and B. Laikhtman, Fermi-liquid properties of a two-dimensional electron system with the Fermi level near a van Hove singularity, Phys. Rev. B **59**, 13592 (1999).

[35] G. Kastrinakis, A Fermi liquid model for the overdoped and optimally doped cuprate superconductors: scattering rate, susceptibility, spin resonance peak and superconducting transition, Physica C **340**, 119 (2000).

[36] A. Hunter, C. Putzke, F. B. Kugler, S. Beck, E. Cappelli, F. Margot, M. Straub, Y. Alexanian, J. Teyssier, A. de la Torre, K. W. Plumb, M. D. Watson, T. K. Kim, C. Cacho, N. C. Plumb, M. Shi, M. Radovic, J. Osiecki, C. Polley, D. A. Sokolov, *et al.*, Non-Fermi liquid quasiparticles in strain-tuned Sr_2RuO_4, arXiv:2503.11311 [cond-mat.str-el].

[37] A. P. Mackenzie, S. R. Julian, A. J. Diver, G. J. McMullan, M. P. Ray, G. G. Lonzarich, Y. Maeno, S. Nishizaki, and T. Fujita, Quantum oscillations in the layered perovskite superconductor Sr_2RuO_4, Phys. Rev. Lett. **76**, 3786 (1996).

[38] N. J. C. Ingle, K. M. Shen, F. Baumberger, W. Meevasana, D. H. Lu, Z.-X. Shen, S. Nakatsuji, Z. Q. Mao, Y. Maeno, T. Kimura, and Y. Tokura, Quantitative analysis of Sr_2RuO_4 angle-resolved photoemission spectra: Many-body interactions in a model Fermi liquid, Phys. Rev. B **72**, 205114 (2005).

[39] H. Iwasawa, Y. Yoshida, I. Hase, S. Koikegami, H. Hayashi, J. Jiang, K. Shimada, H. Namatame, M. Taniguchi, and Y. Aiura, Interplay among Coulomb interaction, spin-orbit interaction, and multiple electron-boson interactions in Sr_2RuO_4, Phys. Rev. Lett. **105**, 226406 (2010).

[40] A. Tamai, M. Zingl, E. Rozbicki, E. Cappelli, S. Riccò, A. de la Torre, S. Mckeown Walker, F. Y. Bruno, P. D. C. King, W. Meevasana, M. Shi, M. Radović, N. C. Plumb, A. S. Gibbs, A. P. Mackenzie, C. Berthod, H. U. R. Strand, M. Kim, A. Georges, and F. Baumberger, High-resolution photoemission on Sr_2RuO_4 reveals correlation-enhanced effective spin-orbit coupling and dominantly local self-energies, Phys. Rev. X **9**, 021048 (2019).

[41] A. P. Mackenzie and Y. Maeno, The superconductivity of Sr_2RuO_4 and the physics of spin-triplet pairing, Rev. Mod. Phys. **75**, 657 (2003).

[42] N. E. Hussey, A. P. Mackenzie, J. R. Cooper, Y. Maeno, S. Nishizaki, and T. Fujita, Normal-state magnetoresistance of Sr_2RuO_4, Phys. Rev. B **57**, 5505 (1998).

[43] T. Katsufuji, M. Kasai, and Y. Tokura, In-plane and out-of-plane optical spectra of Sr_2RuO_4, Phys. Rev. Lett. **76**, 126 (1996).

[44] Y. Sidis, M. Braden, P. Bourges, B. Hennion, S. Nishizaki, Y. Maeno, and Y. Mori, Evidence for incommensurate spin fluctuations in Sr_2RuO_4, Phys. Rev. Lett. **83**, 3320 (1999).

[45] M. Braden, Y. Sidis, P. Bourges, P. Pfeuty, J. Kulda, Z. Mao, and Y. Maeno, Inelastic neutron scattering study of magnetic excitations in Sr_2RuO_4, Phys. Rev. B **66**, 064522 (2002).

[46] F. Servant, B. Fåk, S. Raymond, J. P. Brison, P. Lejay, and J. Flouquet, Magnetic excitations in the normal and superconducting states of Sr_2RuO_4, Phys. Rev. B **65**, 184511 (2002).

[47] M. Braden, P. Steffens, Y. Sidis, J. Kulda, P. Bourges, S. Hayden, N. Kikugawa, and Y. Maeno, Anisotropy of the incommensurate fluctuations in Sr_2RuO_4: A study with polarized neutrons, Phys. Rev. Lett. **92**, 097402 (2004).

[48] K. Iida, M. Kofu, N. Katayama, J. Lee, R. Kajimoto, Y. Inamura, M. Nakamura, M. Arai, Y. Yoshida, M. Fujita, K. Yamada, and S.-H. Lee, Inelastic neutron scattering study of the magnetic fluctuations in Sr_2RuO_4, Phys. Rev. B **84**, 060402(R) (2011).

[49] K. Jenni, S. Kunkemöller, P. Steffens, Y. Sidis, R. Bewley, Z. Q. Mao, Y. Maeno, and M. Braden, Neutron scattering studies on spin fluctuations in Sr_2RuO_4, Phys. Rev. B **103**, 104511 (2021).

[50] D. Thuillier, S. Ghosh, B. J. Ramshaw, and T. Scaffidi, Multipolar Fermi surface deformations in Sr_2RuO_4 probed by resistivity and sound attenuation: A window into electron viscosity and the collision operator, Phys. Rev. Lett. **135**, 146302 (2025).

[51] S. Ghosh, A. Shekhter, F. Jerzembeck, N. Kikugawa, D. A. Sokolov, M. Brando, A. P. Mackenzie, C. W. Hicks, and B. J. Ramshaw, Thermodynamic evidence for a two-component superconducting order parameter in Sr_2RuO_4, Nat. Phys. **17**, 199 (2021).

[52] M. E. Barber, F. Lechermann, S. V. Streltsov, S. L. Skornyakov, S. Ghosh, B. J. Ramshaw, N. Kikugawa, D. A. Sokolov, A. P. Mackenzie, C. W. Hicks, and I. I. Mazin, Role of correlations in determining the Van Hove strain in Sr_2RuO_4, Phys. Rev. B **100**, 245139 (2019).

[53] V. Sunko, E. Abarca Morales, I. Marković, M. E. Barber, D. Milosavljević, F. Mazzola, D. A. Sokolov, N. Kikugawa, C. Cacho, P. Dudin, H. Rosner, C. W. Hicks, P. D. C. King, and A. P. Mackenzie, Direct observation of a uniaxial stress-driven Lifshitz transition in Sr_2RuO_4, npj Quantum Mater. **4**, 46 (2019).

[54] B. Burganov, C. Adamo, A. Mulder, M. Uchida, P. D. C. King, J. W. Harter, D. E. Shai, A. S. Gibbs, A. P. Mackenzie, R. Uecker, M. Bruetzam, M. R. Beasley, C. J. Fennie, D. G. Schlom, and K. M. Shen, Strain control of fermiology and many-body interactions in two-dimensional ruthenates, Phys. Rev. Lett. **116**, 197003 (2016).

[55] C. Bergemann, A. P. Mackenzie, S. Julian, D. Forsythe, and E. Ohmichi, Quasi-two-dimensional Fermi liquid properties of the unconventional superconductor Sr_2RuO_4, Adv. Phys. **52**, 639 (2003).

[56] M. Zingl, J. Mravlje, M. Aichhorn, O. Parcollet, and A. Georges, Hall coefficient signals orbital differentiation in the Hund's metal Sr_2RuO_4, npj Quantum Mater. **4**, 35 (2019).

[57] H. Suzuki, L. Wang, J. Bertinshaw, H. U. Strand, S. Käser, M. Krautloher, Z. Yang, N. Wentzell, O. Parcollet, F. Jerzembeck, *et al.*, Distinct spin and orbital dynamics in Sr_2RuO_4, Nat. Commun. **14**, 7042 (2023).

[58] F. B. Kugler, M. Zingl, H. U. R. Strand, S.-S. B. Lee, J. von Delft, and A. Georges, Strongly correlated materials from a numerical renormalization group perspective: How the Fermi-liquid state of Sr_2RuO_4 emerges, Phys. Rev. Lett. **124**, 016401 (2020).

[59] C. Hodges, H. Smith, and J. W. Wilkins, Effect of Fermi surface geometry on electron-electron scattering, Phys. Rev. B **4**, 302 (1971).

[60] P. Bloom, Two-dimensional Fermi gas, Phys. Rev. B **12**, 125 (1975).

[61] D. Coffey and K. S. Bedell, Nonanalytic contributions to the self-energy and the thermodynamics of two-dimensional Fermi liquids, Phys. Rev. Lett. **71**, 1043 (1993).

[62] G. Palle, C. Hicks, R. Valentí, Z. Hu, Y.-S. Li, A. Rost, M. Nicklas, A. P. Mackenzie, and J. Schmalian, Constraints on the superconducting state of Sr_2RuO_4 from elastocaloric measurements, Phys. Rev. B **108**, 094516 (2023).

[63] Y. Luo, A. Pustogow, P. Guzman, A. P. Dioguardi, S. M. Thomas, F. Ronning, N. Kikugawa, D. A. Sokolov, F. Jerzembeck, A. P. Mackenzie, C. W. Hicks, E. D. Bauer, I. I. Mazin, and S. E. Brown, Normal state ^{17}O NMR studies of Sr_2RuO_4 under uniaxial stress, Phys. Rev. X **9**, 021044 (2019).

[64] https://github.com/BDCurrie/StrainedSr2RuO4ScatteringRatesData.